Biomimetic hierarchical micro/nano texturing of TiAlV alloys by femtosecond laser processing for the control of cell adhesion and migration

M. Martínez-Calderon,[1,2] R. J. Martín-Palma [○],[3,4,*] A. Rodríguez,[1,2] M. Gómez-Aranzadi,[1,2] J. P. García-Ruiz,[5]
S. M. Olaizola,[1,2] and M. Manso-Silván [○][3,4]

[1]*CEIT-Basque Research and Technology Alliance (BRTA), Manuel Lardizábal 15, 20018 Donostia/San Sebastián, Spain*
[2]*Universidad de Navarra, Tecnun, Manuel Lardizábal 13, 20018 Donostia/San Sebastian, Spain*
[3]*Departamento de Física Aplicada, Universidad Autónoma de Madrid, Campus de Cantoblanco, 28049 Madrid, Spain*
[4]*Instituto Universitario de Ciencia de Materiales "Nicolás Cabrera," Universidad Autónoma de Madrid,*
Campus de Cantoblanco, 28049 Madrid, Spain
[5]*Departamento de Biología Molecular, Universidad Autónoma de Madrid, Campus de Cantoblanco, 28049 Madrid, Spain*

The control of the interaction between materials and biological tissues is a key factor to optimize the overall performance of implants and prostheses integrated into the body. With this objective in mind, biomimetic hierarchical one- and two-dimensional surface patterns textured at the micro and nano scales were fabricated on titanium alloys using femtosecond laser processing. The experimental results show that laser irradiation promotes surface oxidation together with a polarization-dependent nano-ripple formation. Human mesenchymal stem cells were subsequently cultured on different surface patterns aiming at determining their response to the underlying micro and nano structures. The ripple topography was demonstrated to induce a nonfouling behavior, which could be exploited in the fabrication of biomimetic hierarchical surface patterns to develop cell-trapping modules.

I. INTRODUCTION

Many outstanding physicochemical properties displayed by natural materials frequently have their origin in a multiscale, hierarchical structure based on a rather small selection of primary constituents. As a matter of fact, materials with radically different properties are found in biological species just by spatially arranging their constituents at different length scales and in different ways [1,2]. In this line, the broad diversity of natural structures serve as inspiration for the design of materials with unusual functionality resulting from their morphology rather than from a change in their chemical composition [3,4]. Moreover, the addition of nano particles to different artificially-designed scaffolds can be used to control cell behaviors such as adhesion or proliferation [5,6].

Several striking examples which can be observed with the naked eye are exemplified by the diversity of colors found in natural organisms, which have led to various practical applications [7–9]. With the previous considerations in mind, in this work the surface of TiAlV was textured at the micro- and nano-scales aiming at using a hierarchical biomimetic approach to control cell attachment, proliferation, and migration. This approach has been followed given the enormous influence of the surface properties of a particular biomaterial on the specific biological response of the surrounding tissues [10,11].

Among the many different surface modification techniques available, femtosecond (fs)-laser micro/nano structuring has been selected given the possibility of structuring the surface of almost any material at the micro scale by means of fs-laser ablation processes [12–14] and at the nano scale thanks to the fabrication of periodic nano patterns, generally termed laser induced periodical surface structures (LIPSS) or ripples [15–19].

For the determination of the biological response of the biomimetic hierarchical surface structures on TiAlV alloys, human mesenchymal stem cells (hMSCs) were chosen. MSCs are capable of differentiating into a large variety of mature cell types, including osteoblasts, chondrocytes, adipocytes, and myoblasts. These cells are receiving increasing attention due to their ability to repair tissue, support hematopoiesis, and to regulate the immune response through the secretion of a variety of cytokines and growth factors [20]. Besides, MSCs can promote in bioreactors the production of different conditioning media with generic interest in regenerative medicine. MSCs secreted factors, such as hormones and micro RNAs, have been identified and related to particular regenerative processes in the vascular endothelium and in musculoskeletal and neurovascular systems [21,22]. Relevantly, these states can be mimicked through specific stimulatory one-, two-, and three-dimensional (1D, 2D, and 3D) structures that regulate cellular adhesion and migration (i.e., cell guiding and trapping structures). Therefore, significant efforts to

---

*Corresponding author: rauljose.martin@uam.es

modify biomaterial surfaces have been recently carried out with very different machining techniques, as previously reviewed [23–26].

Several studies can be found in the literature dealing with the behavior of different cell lines over hierarchical structures at the micro and nano scales fabricated by fs-laser processing. For example, the ability of fs-laser structured surfaces with micro pits and ripples to increase osteogenesis and inhibit adipogenesis of MSCs has been proven [27]. Additionally, it was demonstrated that fs-laser texturing of titanium with different nano patterns can induce the stretching of human MSCs (hMSCs) and potentially improve osteoblastic differentiation [28]. Besides the behavior of murine mesenchymal cells cultured on fs-laser textured surfaces with depths between 1 and 10 μm and widths between 25 and 75 μm covered by LIPSS was analyzed [29]. In this study, it was found that cells are more sensitive to LIPSS than to micro-scale patterns, unless the size of the micro structures is close to the size of the cell and deeper than 5 μm. Finally, it was recently shown how fs-laser micro and nano structuring of ceramics can modulate cell attachment, alignment, and proliferation, leading to the conclusion that hMSCs undergo a faster and greater osteogenic differentiation thanks to this particular structuring technique [30]. In all, it can be established that the specific cell response to the different topographies fabricated by fs-laser structuring depends critically on the cell line to study, with the common finding that LIPSS patterns may help to potentiate certain cell behaviors such as migration and even control cell adhesion, which are key factors when osseointegration is considered. For all these reasons, further studies on this topic are necessary to broaden the knowledge on the biomedical potential of this advanced micro/nano machining technique.

In previous works we have studied cell adhesion and migration on biomimetic hierarchical micro/nano patterns on Si/porous silicon [31–34] and on stainless steel [35]. Cell culture experiments with hMSCs allowed concluding that the biomimetic hierarchical patterns are able to sense the surface nano topographies and orient in specific directions. In the present work, one- and two-dimensional biomimetic hierarchical surface micro/nano patterns were fabricated on titanium alloys using fs-laser irradiation, given that these alloys have a full record of successful *in vivo* implantation, mostly as an endoskeletal substitute [36]. The popularity of titanium-based alloys is primarily due to their good mechanical properties, their corrosion resistance, and their excellent biocompatibility [37], attributed to the formation of stable oxide layers on their surfaces. The influence of different biomimetic hierarchical surface patterns on cell culture viability, migration, and morphology was studied using hMSCs.

II. EXPERIMENT

A. Materials

Commercial Ti6Al4V alloy foils 0.5 mm thick were processed to obtain samples with an area of 100 mm^2. This material was chosen since it is widely used for load bearing prostheses in which good mechanical properties are crucial. Before laser processing, the samples were specular polished using SiC paper of increasing index, cleaned during 10 min in
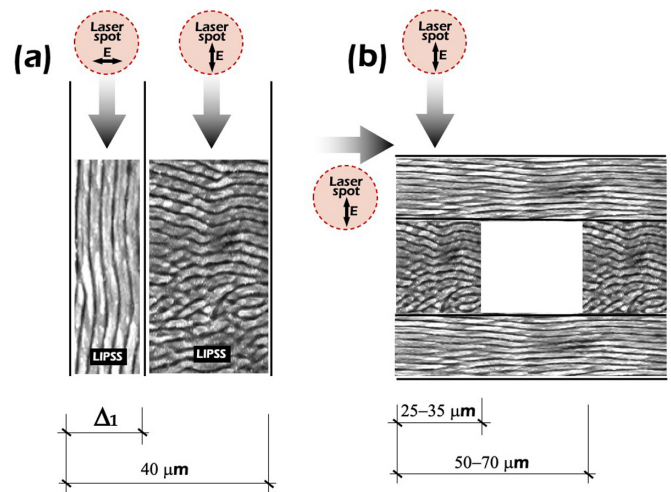

FIG. 1. Scheme of the biomimetic hierarchical patterning models fabricated to analyze cell behavior in (a) one and (b) two dimensions.

an ultrasonic acetone bath, followed by a 10-min ethanol bath. The cleaning process was repeated after LIPSS processing.

B. Fabrication of the biomimetic hierarchical surface micro patterns textured at the nano scale

Micro/nano machining processes were performed in open air atmosphere with a Ti:sapphire laser system consisting of a mode-locked oscillator and a regenerative amplifier. The system delivered up to 2-mJ, 130-fs pulses at a central wavelength of 800 nm, with a 1 kHz repetition rate.

The pulse energy was adjusted with a two-step setup: a variable attenuator formed by a half-wave plate and a low dispersion polarizer and neutral density filters. The laser spot was focused on the titanium alloys by means of a broadband 10× microscope objective with a NA of 0.16. Afterwards, the spot size on the samples was measured using a 50× microscope objective and a Coherent LaserCam HR-UV, yielding approximately a focused spot diameter (ω_0) of 5.5 μm at 800 nm.

Aiming at modifying the structured geometries, the controlled laser defocusing technique was used. This technique has been successfully employed for different nano-structuring applications and allows us to position the sample at different regions of the Gaussian beam distribution and in this way to modify the machined area [38–40]. Therefore, the focusing point was displaced yielding different values of the spot diameter (ω_z) and consequently different machined line-widths [41]. It is important to remark that the actual diameter of a micro-machined line depends on the material's ablation threshold under the employed experimental conditions and is therefore not always identical to the beam diameter [42].

As shown in Fig. 1, two different nano-structuring models were selected. For the fabrication of one-dimensional (1D) biomimetic hierarchical surface patterns [Fig. 1(a)] the period was fixed to 40 μm based on previous studies [35] and the width of the stripes with longitudinal LIPSS (Δ_1) was selected to be approximately 10, 20, or 30 μm by changing the processing parameters. For the fabrication of two-dimensional (2D) surface patterns [Fig. 1(b)] the period was adjusted to be 50 or

TABLE I. Selected processing parameters to achieve the desired structuring geometries.

Fluence (J/cm^2)	Defocusing distance (μm)	Number of pulses per spot	Measured linewidth (μm)
0.42	80	11	20
0.35	90	17	25
0.27	110	20	30
0.21	130	27	35

70 μm and the width of the stripes approximately 25 or 35 μm respectively, achieving squared nontreated areas surrounded by LIPSS patterns of different size to analyze its influence on cell behavior. Finally, the LIPSS orientation (transversal or longitudinal to the micro stripes) was controlled by introducing a half-wave plate before the focusing lens and rotating the laser polarization 90°.

LIPSS nano patterns or stripes with different width while maintaining a good nano-structuring quality were fabricated by adjusting the laser processing parameters. The scanning speed was fixed to 1.5 mm/s and the fluence and spot diameter (ω_z), were adjusted as presented in Table I. The processing parameters for LIPSS fabrication of high homogeneity and definition at different linewidths were selected after a deep study of this phenomenon on TiAlV surfaces. The spatial period of the LIPSS nano patterns was measured to be approximately 560 nm and was maintained fairly constant for all the tested conditions in this work. In addition, as demonstrated in previous works, these LIPSS nano patterns in different metallic materials present a depth ranging from 150 to 250 nm [15,35,43]. For the subsequent surface characterization by XPS and WCA, homogeneously LIPSS-processed TiAlV samples were additionally processed over 0.6 $\times$ 0.6 cm^2 areas.

C. Characterization techniques

A 3D field-emission scanning electron microscope (FE-SEM) system supplied by FEI was used to study the topography of the micro-metric patterns textured at the nano scale. X-ray photoelectron spectra (XPS) were acquired in a SPECS GmbH spectrometer with monochromatic Al-$K\alpha$ x rays ($h\nu = 1486.6$ eV) and normal photoelectron take-off angle (40 eV pass energy). The data were analyzed using CasaXPS v16R1 (Casa Software, UK) taking the C1s C-C contribution at 285.00 eV as binding energy (BE) origin, using combined Gaussian-Lorentzian envelopes with $G/L = 30$ and Shirley background subtraction. All quantitative data refer to the statistical analyses at three different points of 0.3 $\times$ 0.3 cm^2. and are expressed as mean value $\pm$ standard error. For the fitting of Ti 2p spectra, constraints were imposed between the area (A) of the 3/2 and 1/2 spin-orbit contributions, allowing a 5% deviation from the expected $A(3/2)/A(1/2) = 0.5$.

Static water contact angle (WCA) measurements were obtained by dispensing 3.5-μl droplets of distilled water with a micro syringe on the sample surface. The whole process was recorded with a digital camera. In order to measure the static WCA, the recorded videos were analyzed using the sessile drop method with the low-bond axisymmetric drop shape analysis (LBADSA) plugin for ImageJ [44]. Successive mea-

surements were reproducible with an average error of $\pm 2°$. All WCA measurements were carried out at room temperature.

The influence of the LIPSS process on the polycrystalline structure of the TiAlV alloy was analyzed by grazing incidence x-ray diffraction (XRD) using a PANanalytical X'Pert MPD system with Cu-$K\alpha$ radiation, incidence angle of 0.5°, and 25–80° 2θ range.

D. Cell culture and analysis.

Human bone marrow samples (2–4 ml) from healthy donors provided by Hospital Universitario La Princesa (Madrid, Spain) were cultured on the Ti-based micro/nano patterns. 70% Percoll centrifugation gradients were prepared to collect the cells and afterwards seeded at 200 000/cm^2 in Dulbecco's modified Eagle's medium with low glucose (DMEM-LG) supplemented with 10% foetal bovine serum (FBS). For the sake of sterilization, the LIPSS on TiAlV were exposed to UV light for 10 min. They were then thoroughly washed with phosphate-buffered saline (PBS) and seeded with 15 000 cells placed in 24 multiwells. hMSCs were incubated with DMEM-LG adjusted to 10% FBS at 37 °C in 5% CO$_2$. After 72 h of culture, the TiAlV plates were washed twice with PBS, and hMSCs were fixed in 3.7% formaldehyde in PBS for 30 min at room temperature (RT). Immune staining was performed by permeating hMSCs in 0.5% Triton X-100 at RT in cytoskeleton CSK buffer (100 mM NaCl, 10 mM Pipes pH 6.8, 3 mM MgCl2, 3 mM EGTA, and 0.3 M sucrose) for 30 min. Then, the surfaces were blocked with 1% bovine serum albumin in PBS for 1 h at RT. Primary reactions were induced with sera from autoimmune mice during 1 h. After washing, the surfaces were incubated in dark conditions for 1 h with Alexa 488 Phalloidin (1:500, Invitrogen) to reveal the actin cytoskeleton and with 40,6-diamidino-2-phenylindole (1:5000, Calbiochem) to stain the nuclei. After incubation, the surfaces were washed, dehydrated with absolute ethanol, and mounted in Mowiol coverslips (Calbiochem). Cells were observed in an inverted fluorescence microscope (Olympus IX81, Olympus Corporation, Shinjuku, Tokyo, Japan) coupled to a charge-coupled device color camera. Image analysis of cell density was performed using ImageJ macros over four fields of every cell culture condition. All methods carried out in this work were approved by the Ethics Committee of the Hospital Universitario La Princesa and fully complied with the governmental requirements. The morphometric study was performed using ImageJ software [44] for filtering and appropriate discrimination functions to provide automated estimations of area and substrate induced polarization. The statistical analyses are based on the response of hMSCs from the same donor to two replicas of each condition and four different fluorescence microscopy fields for each replica.

TABLE II. Details of the surface stoichiometry of as-polished and LIPSS-processed TiAlV alloys as determined from XPS survey spectra (maximum error of ± 0.6 at.%) and details of the bonding chemistry for C, O, and Ti (maximum error of ± 0.8%) extracted from the C 1s, O 1s, and Ti 2p core-level spectra.

Element (at.%) Sample	C			N	O		Ti			Al	V
	C-C	C-O	C=O		O_2^-	CO_3	Ti	TiO_x	TiO_2		
As-polished		61.3		1.5	25.9			7.1		4.0	0.2
	90.7	3.9	5.4		48.3	51.3	5.3	4.3	90.4		
LIPSS		38.3			41.2			10.8		9.4	0.3
	57.4	34.4	8.2		54.8	45.2	0.8	1.4	97.8		

III. RESULTS AND DISCUSSION

One- and two-dimensional biomimetic hierarchical micro patterns textured at the nano scale were fabricated on TiAlV substrates following the procedure described in Sec. II. Adhesion and migration of human mesenchymal stem cells (hMSCs) on the Ti-based 1D and 2D patterns were subsequently analyzed. In the following sections we present the key experimental results.

A. Surface chemistry of TiAlV upon LIPSS processing

The evolution of the surface chemistry upon LIPSS patterning was monitored by XPS on as-polished and homogeneously laser-processed TiAlV substrates. We first compared the general stoichiometry of the surface by performing wide scan spectra. The surface of both as-polished and structured TiAlV surfaces denoted the presence of C, O, Al, Ti, and V, plus a contribution of N in the as-polished substrates. The details of the stoichiometry for the two different surfaces are detailed in Table II. Relevantly, the main differences between irradiated and nonirradiated surfaces concern surface passivation components. Prior to laser structuring, the surface contains mainly C and O, with a Ti surface composition well below 10 at.%. After LIPSS processing, the C surface

composition is reduced by circa 35% accompanied by a notable increase of O, which becomes the dominant surface composition element. All of the observed transformations are coherent with a process performed in atmospheric conditions at extremely high local temperatures. The amount of surface Ti increases also notably, although the 100% increase of Al content is the most remarkable aspect from the point of view of the alloy constituents. The segregation of Al at the grain boundaries is a well-known effect on ternary TiAlMe alloys, as well as the enhancement of this effect upon thermal processing [45].

The evolution of the surface composition presented also relevant features from the point of view of the bonding chemistry. The C 1s, O 1s, and Ti 2p core-level spectra for the as-polished and LIPSS-processed surfaces are portrayed in Fig. 2. With respect to the C 1s core level [Fig. 2(a)], the surface chemistry is dominated by three main components related to C-C at a binding energy (BE) of 285.0 eV, to C-O at 286.4 eV, and to C = O at 288.5 eV. However, the surface modification of C is dramatic upon LIPSS processing and the intermediate component, influenced by the C-N bonding for the as-polished samples, gives rise to a high BE shift (+1.0 eV) as N species are eliminated upon LIPSS patterning (all the relative changes in the bonding composition are
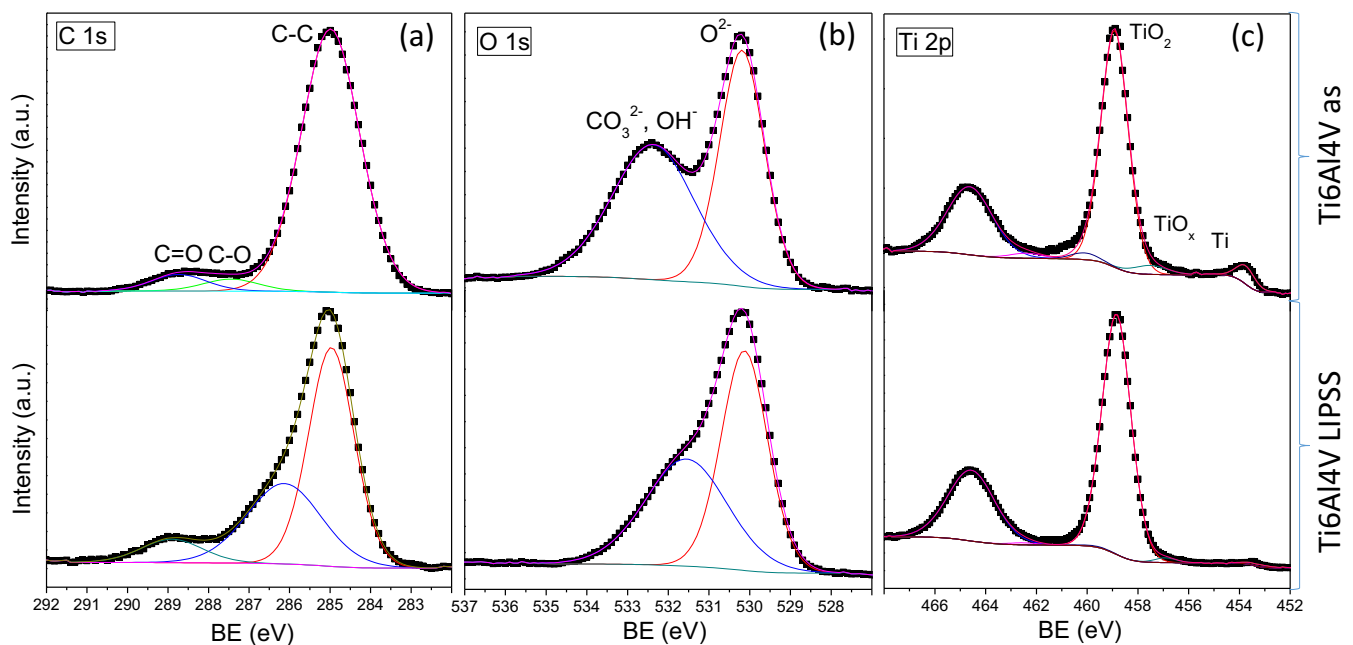

FIG. 2. C 1s (a), O 1s (b), and Ti 2p (c) core-level spectra from as-polished (top) and LIPSS-processed (bottom) TiAlV surfaces.
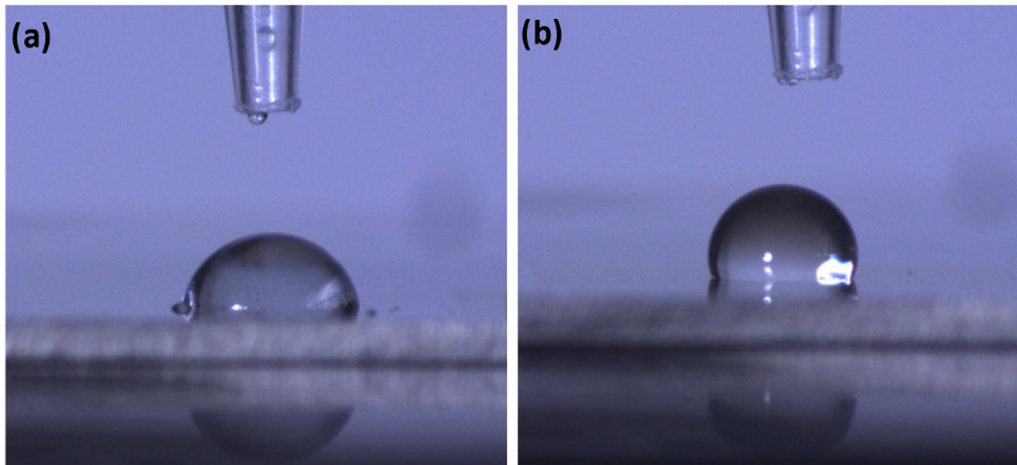
FIG. 3. WCA on (a) an as-polished TiAlV substrate and (b) LIPSS-processed TiAlV.

also presented in Table II). The highest BE component also experiences a slight shift to higher BE (+0.5 eV), which suggests the additional formation of highly oxidized C species (O−C = O).

The O $1s$ core-level spectra from the surfaces of the TiAlV alloys are presented in Figs. 2(b), which complement the information already obtained from the C $1s$ spectra. Two main contributions can be considered, one referring to the presence of carbonate and hydroxide species (wider contribution at 532.4 eV) and the second one to the stoichiometric titanium oxide (at 530.2 eV). Upon LIPSS pattering, this latter composition increases considerably its relative composition (see Table II for details), which is in agreement with the already mentioned stoichiometric increase of both Ti and O. Additionally, the highest BE component suffers a low binding energy shift, which is coherent with an increase of the carbonate load with respect to the hydroxyl upon high-temperature processing.

From the Ti $2p$ core level spectra [Fig. 2(c)] three main contributions are identified, which are doubled in the resolved $2p^{3/2}$ and $2p^{1/2}$ spin-orbit splitting. For brevity, the description of the positions of the peaks is restricted to the $2p^{3/2}$ component. The as-polished surfaces are dominantly composed of stoichiometric titania (458.8 eV), although there is also a component from substoichiometric titania (457.5 eV) and a contribution from metallic Ti in the alloy (453.7 eV) [46]. This latter component is clearly identified in as-polished TiAlV surfaces by the peak low BE peak and the associated increase of photoelectron background from the associated yield energy. The two lower BE components suffer a drastic decrease of intensity upon LIPSS processing, leading to an almost consolidated stoichiometric titania (see Table II). Overall, the results suggest a notable increase of oxidized species on the metallic alloy after LIPSS processing with a remarkable depletion of expected Ti content (90% in the alloy) in favor of O, C, and Al.

B. LIPSS induced changes in surface wettability

Surface wettability has been demonstrated to play a crucial role in cell binding processes by conditioning the adsorption of medium proteins and their interaction with cellular integrins. The general conclusion extracted from most of the studies is that a higher water contact angle (WCA) leads to lower cell adhesion [28,29,47]. However, caution should be taken to avoid the use of WCA as an absolute determinant of biofouling [48]. In spite of the previous observations, we performed WCA experiments over samples textured with continuous LIPSS patterns and as-polished TiAlV samples (Fig. 3) given the influence of surface wettability on biocompatibility. As expected, these measurements allowed us to conclude that LIPSS-processed areas show a hydrophobic behavior with a typical WCA of 115 ± 2°, while pristine TiAlV shows a hydrophilic behavior with a WCA of 70 ± 2°.

C. Fabrication of 1D and 2D biomimetic hierarchical micro patterns

The row of images in Fig. 4 shows the typical surface morphology of the one-dimensional biomimetic hierarchical micro patterns textured at the nano scale fabricated by LIPSS processing. It is observed that the nano-patterned surfaces with different LIPSS orientation show a good degree of homogeneity. It is also perceived that the 90° polarization rotation has been effectively achieved, resulting in micro stripes with alternating LIPSS nano patterns. The transition between the longitudinal (with LIPSS ripples parallel to the micro stripe) and transverse patterning (with LIPSS ripples perpendicular to the micro stripe) are sharp and leave no open space to nonirradiated areas. This is consistently observed on the surfaces with 10-, 20-, and 30-μm-wide longitudinal micro stripes shown in Figs. 4(a)–4(c), respectively.

Two-dimensional (2D) biomimetic hierarchical structures were, on the other hand, designed to present simultaneously contrasting nonirradiated and LIPSS structures in such a way that one side of the nonirradiated squared islands is parallel to the LIPSS surrounding nano ripples and the other side is perpendicular. These structures can be clearly identified in Figs. 5(a) and 5(b) for total square + stripe periodicities of 50 and 70 μm, respectively. The main image helps to visualize the geometry and scale of each structure, while the higher magnification illustrates the orientation of the LIPSS ripples
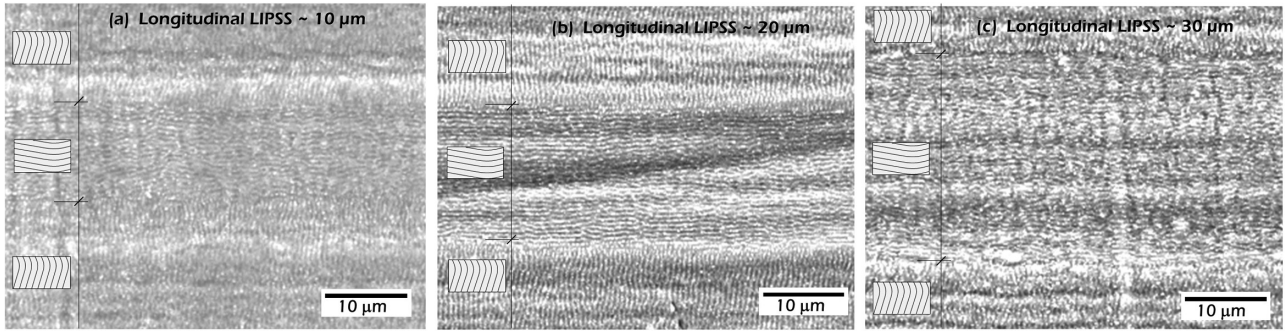
FIG. 4. Scanning electron microscopy (SEM) images of the biomimetic hierarchical surfaces showing the 1D structuring strategy with different geometries and feature sizes. The width of the lines filled with longitudinal LIPSS is (a) 10 μm, (b) 20 μm, and (c) 30 μm.

with respect to each of the sides of the unirradiated squared islands.

In order to identify any potential changes in the phases present on the Ti6Al4V alloys, we performed a glancing angle XRD study of the various surfaces. The results demonstrated that the different laser irradiation processes do not substantially change the phases present on the alloy (equilibrium of α to β phases) [49]. Furthermore, the results confirm that the oxidation of the surface is limited and does not lead to an identifiable amount of any titanium oxide phases. In the XRD diffractograms the vertical discontinuous line identifies the presence of the (110) peak of the minor body centered cubic (bcc, β) phase. The presence of the phase is identified by the

clear asymmetry of the (101) peak of the dominant hexagonal closed packed (hcp, α) phase [50].

D. hMSCs adhesion to the 1D and 2D biomimetic hierarchical surface patterns

To analyze cell behavior on the 1D and 2D biomimetic hierarchical surface structures, hMSCs were cultured on the different LIPSS-processed patterns as well as on control surfaces. In the case of the 1D structures, the periodicity was 40 μm and longitudinal LIPSS stripes with 10-, 20-, and 30-μm width were considered. The cell adhesion results, depicted in Fig. 6, are presented with blue saturation images (top), which
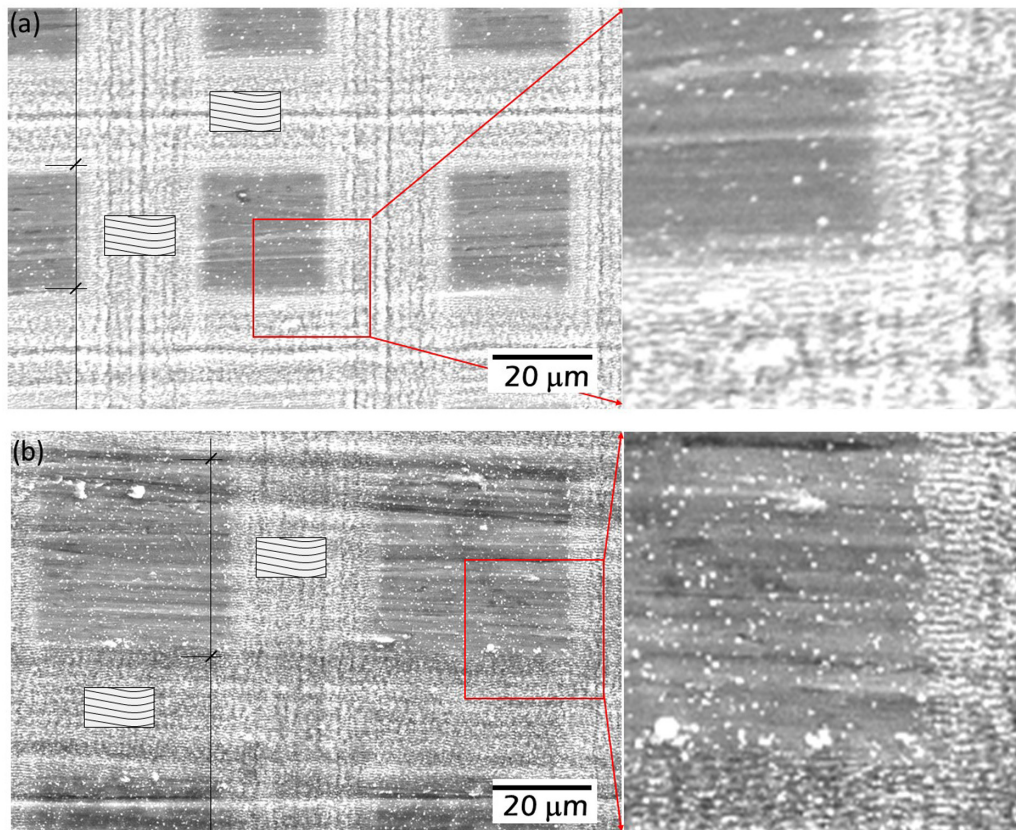

FIG. 5. SEM images of the nano-structured surfaces with the 2D structuring strategy with different geometries accounting for flat square + LIPSS stripe periodicities of (a) 50 and (b) 70 μm.
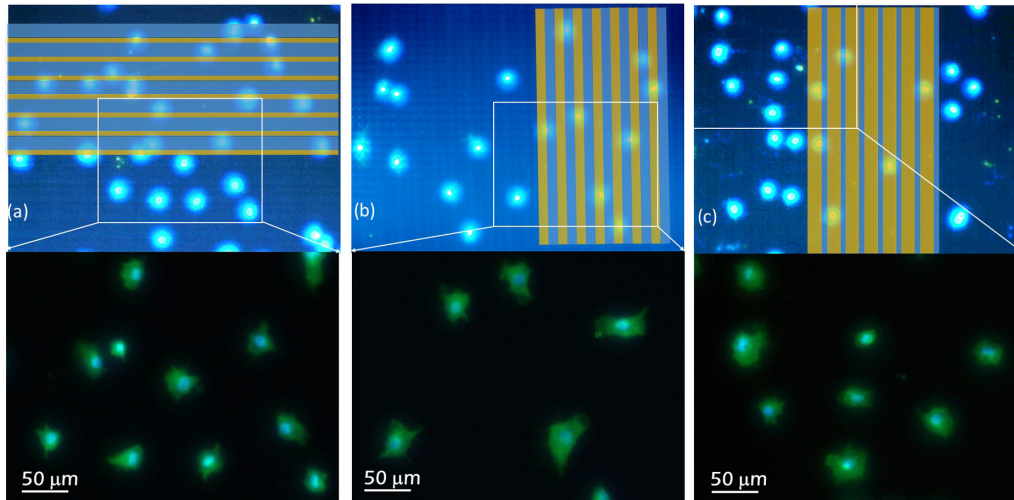
FIG. 6. Fluorescence microscopy images of hMSCs cultured on various biomimetic hierarchical 1D TiAlV micro patterns with longitudinal LIPSS stripes (a) 10 μm, (b) 20 μm, and (c) 30 μm wide. Top: general view with saturated nuclear staining for identification of periodicity. Bottom: Higher magnification image of the cellular adhesion characteristics. Blue: nuclear staining with DAPI. Green: actin cytoskeleton staining with 488 phalloidin.

allow discriminating the underlying pattern (note additional semitransparent mask to guide the eye), and merged nuclear and actin cytoskeleton staining at higher magnification (bottom).

The experimental results show that no cell polarization takes place as deduced from the characteristic rounded shape of the cells irrespective of the LIPSS configuration considered. Besides, the cells do not show a preference for a particular stripe structure and display a stochastic nuclear apposition. A morphometric study on the cells shows that there is either no difference in the mean actin cytoskeleton expansion area (610, 660, and 630 $\pm$ 80 μm^2 for longitudinal LIPSS stripes of 10, 20, and 30 μm, respectively). The expansion area is in fact restricted by the lack of cellular extensions (note the short length of the few observable filopodia) and the general constriction of the acting cytoskeleton to perinuclear areas. This behavior is in stark contrast to that observed in stainless-steel based structures [35], where hMSCs showed a clear trend to align along longitudinal LIPSS stripes. Thus, the experimental results evidence that for LIPSS stripes on TiAlV the nano topography induces a poor adhesive and expansive response of hMSCs. Relevantly, this kind of response has already been described for alternative nano topography rich titania (TiO$_2$) suggesting that nano-rough areas of this transition-metal oxide lead to antifouling properties [51,52].

According to different models describing cell migration, the absence of any preferred orientation/polarization of hMSCs on 1D LIPSS-processed TiAlV alloys suggests that these surfaces are not prone to induce cell guiding effects, which are relevant in very different cellular processes and most relevantly for therapeutic wound healing processes. As such, in view of these results, 2D hierarchical structures were fabricated with nonirradiated areas that could complement the nonfouling behavior observed on LIPSS nano-roughened areas.

Figure 7 portrays the response of hMSCs to the biomimetic hierarchical TiAlV surfaces processed with 2D LIPSS. From the point of view of nuclear apposition, hMSCs show an apparent trend to locate at nonirradiated islands. This effect is not dramatic for the smallest nonirradiated TiAlV islands of 25 $\times$ 25 μm^2 [Fig. 7(a), top], but becomes drastic for the larger islands of 35 $\times$ 35 μm^2 [Fig. 7(b), top]. A statistical analysis of the surface cell distribution shows that in the first case 58 $\pm$ 6% of nuclei locate on the TiAlV square islands while this number increases to 81 $\pm$ 6% for the larger islands. The corresponding fluorescence microscopy images showing the actin cytoskeleton [Figs. 7(a) and 7(b), bottom] clearly illustrate the influence of the topographic contrasts on cell adhesion. The nonirradiated areas become active sites for cellular binding, which gives rise to some cellular polarization effects in the case of the smaller TiAlV islands [Figs. 7(a)], even though the polarization angle cannot be directly related to the underlying micro or nano-topographic orientation. In the case of TiAlV structures with larger square islands, a trend to constrict the cellular areas to the size of the squares is visibly identified [Fig. 7(b)]. From the morphometric study, the mean expansion area of the cells in the case of smaller squares is 2100 $\pm$ 600 μm^2, while for the larger squares the area is reduced to 1100 $\pm$ 200 μm^2. This contrast in the area of adhesion suggests that there is a threshold between the smaller and larger TiAlV squares which influences the final conformation. hMSCs cultured on the smaller squares cannot constrict to such small areas and expand, passing over LIPSS nano-topographic areas to find additional TiAlV squares where to adhere. Meanwhile, most of the cells cultured on the larger areas find enough surface to constrain to a single square and limit the tendency of the cells to form filopodia farther than the area of the squares. In this case, the LIPSS surrounded TiAlV islands play a cell trapping role. The lower relative value of the standard deviation of the expansion area
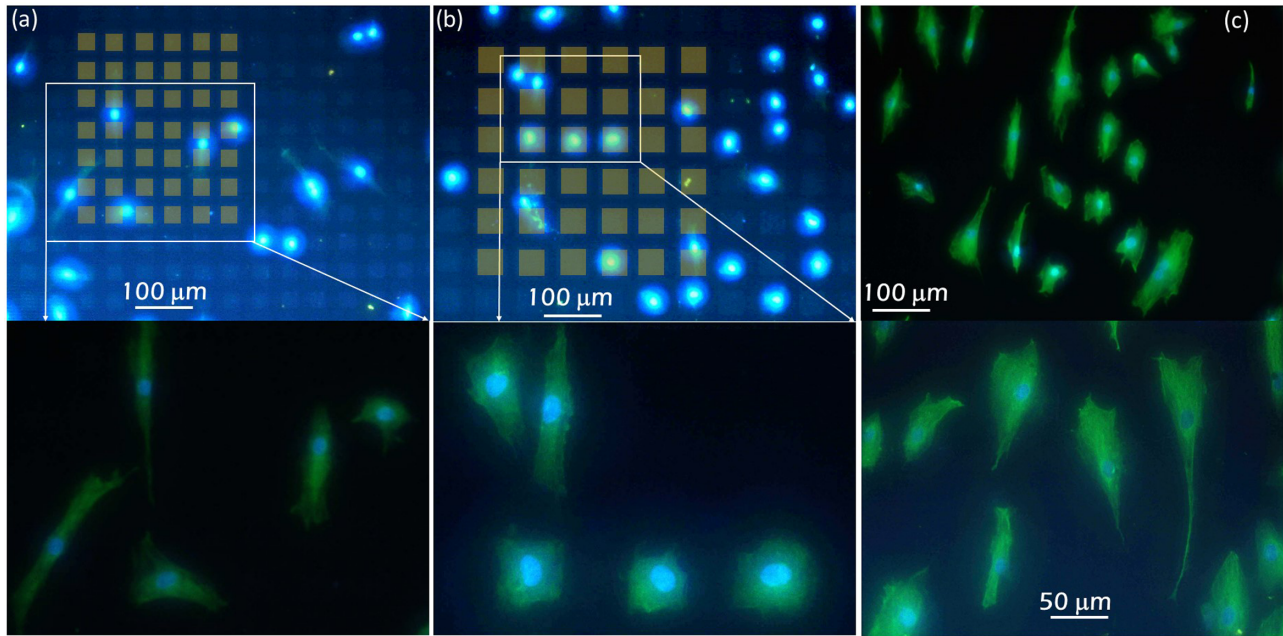
FIG. 7. Fluorescence microscopy images of hMSCs cultured on 2D biomimetic hierarchical TiAlV micro patterns with LIPSS frame and nonirradiated squared islands of (a) 25 μm and (b) 35 μm side. (c) Fluorescence microscopy images of hMSCs cultured on as-polished TiAlV control substrates. Top: general view [nuclear staining in saturation for (a) and (b)] for identification of the general morphology. Bottom: Higher magnification image of the cellular adhesion characteristics. Blue: nuclear staining with DAPI. Green: actin cytoskeleton staining with 488 phalloidin.

of the cells further suggests this role, as the trap dimensions tend to become the mode for the adhesion of the cells.

Figure 7(c) shows fluorescence microscopy images for hMSCs cultured on nonirradiated TiAlV surfaces used as cell adhesion controls. The images demonstrate that in this case the cells find binding sites where they can develop stronger focal adhesions and expand to larger areas ($2600 \pm 800 \, \mu m^2$). Irrespective of the quite large variation of the adhesion area the cells are able to develop filopodia and present rather elongated-polygonal shapes, especially when compared with cells cultured on 1D structures.

The overall cell adhesion results confirm the relevant role of surface tension micro contrasts in the governance of biofouling processes. Relevant for this work, the different hydrophobic/hydrophilic properties, as determined by WCA measurements, appear to be counterintuitive with respect to their tendency to favor or inhibit the adhesion of hMSCs. In fact, we observe that the more hydrophilic areas are domains where the cells find bonding sites and develop strong focal adhesions. Inversely, the hydrophobic areas behave as nonfouling domains and drastically impede the formation of filopodia. Such exotic fouling behavior is in agreement with previous observations. It has been highlighted that different hydrophilic chemistries or the presence of micro-nano topographies (from the point of view of the material surface) or the type of cell or the time given for cell-surface interaction (from the point of view of the biological system) give rise to notable changes in cell adhesion trends [48]. From the point of view of Ti-based nano materials, it has been already shown that TiO_2 structures passivate the surface, inducing strong local hydrophobicity, and this derives to steric hindrance effects when polar residues from proteins interact with the surfaces. As adhesive eukary-

ote cells, hMSCs require the formation of focal adhesions to fulfil all their functions. For this, they require the interaction of transmembrane polar proteins (integrins) with different moieties on the substrate. Importantly, the high hydrophobic character of nano-rough TiO_2 prevents, at least in the first stages of cell-titania interaction, an appropriate conformation of mediating proteins, and thus limit polar-polar interactions between the cell and the surface required for the formation of focal adhesions. The consequence is thus antifouling surfaces, at least in the short term of the experimental conditions studied in this work (cell culture time of 72 h).

IV. CONCLUSIONS

Biomimetic hierarchical surface patterns were fabricated by femtosecond (fs) laser micro/nano machining technology on Ti6Al4V alloys, with the objective of expanding previous knowledge regarding how these patterns can be used to control cell behavior. The micro patterns consisted of 1D micro stripes with internal LIPSS-induced nano ripples that alternate orientation with respect to the micro stripe direction (i.e., one longitudinal, next transversal). Additionally, 2D structures consisting of LIPSS frames delimiting pristine TiAlV squares were also fabricated.

The formation of LIPSS ripples on TiAlV alloys has been found to increase the degree of surface oxidation further than what was observed for the native oxide of the pristine TiAlV alloys. This, in addition to the induced nano-topographic modification, leads to a remarkable change of surface tension. In fact, a transition is induced by LIPSS processing from a hydrophilic to a hydrophobic surface (water contact angles

of 70 and 115°, respectively), which suggests a potential influence in the subsequent response of cell cultures.

Human mesenchymal stem cells (hMSCs) were used to probe the biofunctionality of the hierarchical LIPSS micro-nano patterns. The experimental results showed that an antifouling effect is induced by the nano-ripple formation, as deduced from the poor expansion area of the cells and lack of development of filopodia. The most relevant results were thus obtained for the biomimetic hierarchical 2D structures, which alternate nano-topographic contrasts (pristine TiAlV squares vs nano-ripple frames). The statistics show that most of the cells constrict to the native TiAlV areas and the morphometric analysis corroborates that their area of expansion converges to the area of the nonirradiated squares.

The experimental results constitute a good example of how surface hierarchical micro-nano structures can influence cell behavior. The particular behavior observed by LIPSS structuring of TiAlV alloys suggests that they cannot only be functional structures for orthopedic devices, but also play an influential role in cell culture devices, such as cell traps, which could be incorporated in bioreactors for the *in vitro* production of factors by hMSCs and other secreting cells under particular nano-topographically designed stimuli. In any case, the generic influence of shape transforming substrates on cell function has been supported for decades [53], which points to further experimental efforts allowing us to evaluate the hMSCs differentiation routes activated by the LIPSS structures designed on TiAlV alloys.

[1] P. Fratzl, T. Speck, and S. Gorb, Bioinspiration Biomimetics **11**, 060301 (2016).

[2] A. Lakhtakia and R. J. Martín-Palma, *Engineered Biomimicry* (Elsevier, Amsterdam, 2013).

[3] P. Fratzl and R. Weinkamer, Prog. Mater. Sci. **52**, 1263 (2007).

[4] C. Sanchez, H. Arribart, and M. M. G. Guille, Nat. Mater. **4**, 277 (2005).

[5] R. Hou, G. Zhang, G. Du, D. Zhan, Y. Cong, and Y. Cheng, J. Fu, Colloids Surf., B **103**, 318 (2013).

[6] F. A. Blyakhman, E. B. Makarova, F. A. Fadeyev, D. V. Lugovets, A. P. Safronov, P. A. Shabadrov, T. F. Shklyar, G. Y. Melnikov, I. Orue, and G. V. Kurlyandskaya, Nanomaterials **9**, 232 (2019).

[7] M. J. Domingue, A. Lakhtakia, D. P. Pulsifer, L. P. Hall, J. V. Badding, J. L. Bischof, R. J. Martín-Palma, Z. Imrei, G. Janik, V. C. Mastro, M. Hazen, and T. C. Baker, Proc. Natl. Acad. Sci. USA **111**, 14106 (2014).

[8] R. J. Martín-Palma and A. Lakhtakia, Appl. Phys. Rev. **4**, 021103 (2017).

[9] R. J. Martín-Palma and M. Kolle, Opt. Laser Technol. **109**, 270 (2019).

[10] K. Anselme, A. Ponche, and M. Bigerelle, Proc. Inst. Mech. Eng., Part H. **224**, 1487 (2010).

[11] S. Pacelli, V. Manoharan, A. Desalvo, N. Lomis, K. S. Jodha, S. Prakash, and A. Paul, J. Mater. Chem. B **4**, 1586 (2016).

[12] B. N. Chichkov, C. Momma, S. Nolte, F. von Alvensleben, and A. Tünnermann, Appl. Phys. A: Mater. Sci. Process. **63**, 109 (1996).

[13] B. Rethfeld, D. S. Ivanov, M. E. Garcia, and S. I. Anisimov, J. Phys. D.: Appl. Phys. **50**, 193001 (2017).

[14] M. Martínez-Calderon, A. Rodríguez, A. Dias-Ponte, M. C. Morant-Miñana, M. Gómez-Aranzadi, and S. M. Olaizola, Appl. Surf. Sci. **374**, 81 (2016).

[15] J. Bonse, S. Hohm, S. V. Kirner, A. Rosenfeld, and J. Kruger, IEEE J. Sel. Top. Quantum Electron. **23**, 1 (2017).

[16] T. J. Y. Derrien, J. Krüger, T. E. Itina, S. Höhm, A. Rosenfeld, and J. Bonse, Appl. Phys. A: Mater. Sci. Process. **117**, 77 (2014).

[17] F. A. Müller, C. Kunz, and S. Gräf, Materials (Basel). **9**, 476 (2016).

[18] M. Martínez-Calderon, J. J. Azkona, N. Casquero, A. Rodríguez, M. Domke, M. Gómez-Aranzadi, S. M. Olaizola, and E. Granados, Sci. Rep. **8**, 14262 (2018).

[19] I. Gnilitskyi, T. J. Y. Derrien, Y. Levy, N. M. Bulgakova, T. Mocek, and L. Orazi, Sci. Rep. **7**, 8485 (2017).

[20] M. D. M. Joel, J. Yuan, J. Wang, Y. Yan, H. Qian, X. Zhang, W. Xu, and F. Mao, Am. J. Transl. Res. **11**, 3890 (2019).

[21] M. Madrigal, K. S. Rao, and N. H. Riordan, J. Transl. Med. **12**, 260 (2014).

[22] H. R. Hofer and R. S. Tuan, Stem Cell Res. Ther. **7**, 131 (2016).

[23] H. J. Jeon, C. G. Simon, and G. H. Kim, J. Biomed. Mater. Res., Part B **102**, 1580 (2014).

[24] M. Nikkhah, F. Edalat, S. Manoucheri, and A. Khademhosseini, Biomaterials **33**, 5230 (2012).

[25] R. K. Das and O. F. Zouani, Biomaterials **35**, 5278 (2014).

[26] P. J. Albert and U. S. Schwarz, Cell Adhes. Migr. **10**, 516 (2016).

[27] V. Dumas, A. Guignandon, L. Vico, C. Mauclair, X. Zapata, M. T. Linossier, W. Bouleftour, J. Granier, S. Peyroche, J. C. Dumas, H. Zahouani, and A. Rattner, Biomed. Mater. **10**, 55002 (2015).

[28] A. Cunha, A. M. Elie, L. Plawinski, A. P. Serro, A. M. Botelho Do Rego, A. Almeida, M. C. Urdaci, M. C. Durrieu, and R. Vilar, Appl. Surf. Sci. **360**, 485 (2016).

[29] O. Raimbault, S. Benayoun, K. Anselme, C. Mauclair, T. Bourgade, A. M. Kietzig, P. L. Girard-Lauriault, S. Valette, and C. Donnet, Mater. Sci. Eng. C **69**, 311 (2016).

[30] A. Carvalho, L. Cangueiro, V. Oliveira, R. Vilar, M. H. Fernandes, and F. J. Monteiro, Appl. Surf. Sci. **435**, 1237 (2018).

[31] V. Torres-Costa, G. Martínez-Muñoz, V. Sánchez-Vaquero, A. Muñoz Noval, L. González-Méndez, E. Punzón-Quijorna, D. Gallach-Pérez, M. Manso-Silván, A. Climent-Font, J. P. García-Ruiz, and R. J. Martín-Palma, Int. J. Nanomed. **7**, 623 (2012).

[32] P. Y. Collart-Dutilleul, E. Secret, I. Panayotov, D. Deville De Périère, R. J. Martín-Palma, V. Torres-Costa, M. Martin, C. Gergely, J. O. Durand, F. Cunin, and F. J. Cuisinier, ACS Appl. Mater. Interfaces **6**, 1719 (2014).

[33] J. Hernández-Montelongo, A. Muñoz-Noval, J. P. García-Ruíz, V. Torres-Costa, R. J. Martín-Palma, and M. Manso-Silván, Front. Bioeng. Biotechnol. **3**, 60 (2015).

[34] A. M. Noval, V. S. Vaquero, E. P. Quijorna, V. T. Costa, D. G. Pérez, L. G. Méndez, I. Montero, R. J. M. Palma, A. C. Font, J. P. G. Ruiz, and M. M. Silván, J. Biomed. Mater. Res., Part A **100A**, 1615 (2012).

[35] M. Martínez-Calderon, M. Manso-Silván, A. Rodríguez, M. Gómez-Aranzadi, J. P. García-Ruiz, S. M. Olaizola, and R. J. Martín-Palma, Sci. Rep. **6**, 36296 (2016).

[36] M. Saini, World J. Clin. Cases **3**, 52 (2015).

[37] H. Tschernitschek, L. Borchers, and W. Geurtsen, J. Prosthet. Dent. **96**, 12 (2006).

[38] G. V. Kurlyandskaya, J. M. Barandiarán, P. Mínguez, and L. Elbaile, Nanotechnology **14**, 1246 (2003).

[39] M. Ohata and N. Furuta, Anal. Sci. **20**, 701 (2004).

[40] Y. Su, R. A. Tong, H. Zhang, P. Liang, C. A. Wang, and M. Zhong, J. Alloys Compd. **787**, 295 (2019).

[41] J. Alda, Laser and Gaussian beam propagation and transformation, in *Encyclopedia of Optical and Photonic Engineering*, 2nd. ed., edited by C. Hoffman and R. Driggers (Taylor & Francis, Boca Raton, 2015).

[42] J. Lehr and A. M. Kietzig, Opt. Lasers Eng. **57**, 121 (2014).

[43] G. Giannuzzi, C. Gaudiuso, R. Di Mundo, L. Mirenghi, F. Fraggelakis, R. Kling, P. M. Lugarà, and A. Ancona, Appl. Surf. Sci. **494**, 1055 (2019).

[44] C. T. Rueden, J. Schindelin, M. C. Hiner, B. E. DeZonia, A. E. Walter, E. T. Arena, and K. W. Eliceiri, BMC Bioinformatics **18**, 529 (2017).

[45] J. A. Jiménez, M. Sanchez-Agudo, G. G. Fuentes, and A. Gutiérrez, Surf. Interface Anal. **33**, 570 (2002).

[46] M. Hannula, H. Ali-Löytty, K. Lahtonen, E. Sarlin, J. Saari, and M. Valden, Chem. Mater. **30**, 1199 (2018).

[47] A. Ranella, M. Barberoglou, S. Bakogianni, C. Fotakis, and E. Stratakis, Acta Biomater. **6**, 2711 (2010).

[48] M. R. Alexander and P. Williams, Biointerphases **12**, 02C201 (2017).

[49] B. Wysocki, P. Maj, R. Sitek, J. Buhagiar, K. J. Kurzydłowski, and W. Świeszkowski, Appl. Sci. **7**, 657 (2017).

[50] See Supplemental Material at http://link.aps.org/supplemental/10.1103/PhysRevMaterials.4.056008 for experimental XRD diffractograms.

[51] D. Gallach Pérez, E. Punzón Quijorna, R. Sanz, V. Torres-Costa, J. P. García Ruiz, and M. Manso Silván, Colloids Surf., B **126**, 146 (2015).

[52] E. Punzón-Quijorna, V. Sánchez Vaquero, S. Rodríguez-López, V. M. De La Prida, A. Climent Font, J. P. García Ruiz, M. Hernandez-Velez, and M. M. Silván, Compos. Interfaces **19**, 251 (2012).

[53] P. A. Watson, FASEB J. **5**, 2013 (1991).